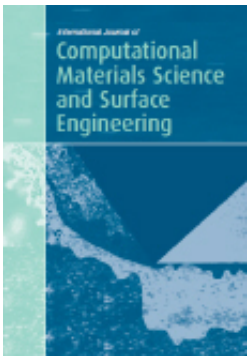

International Journal of Computational Materials Science and Surface Engineering

ISSN online: 1753-3473 - ISSN print: 1753-3465
https://www.inderscience.com/ijcmsse

Computational and experimental analysis of partly coated hydrophobic airfoil

Suresh Chandra Khandai, S. Prasath, B. Naveen

DOI: 10.1504/IJCMSSE.2023.10058150

Article History:

Received:	18 June 2022
Last revised:	02 November 2022
Accepted:	15 November 2022
Published online:	08 January 2024

Computational and experimental analysis of partly coated hydrophobic airfoil

Suresh Chandra Khandai, S. Prasath and B. Naveen*

Department of Aeronautical Engineering,
Rajalakshmi Engineering College,
Chennai, 602105, India
Email: sureshchandrakhandai@rajalakshmi.edu.in
Email: prasath.s.2018.aero@rajalakshmi.edu.in
Email: naveen.b.2018.aero@rajalakshmi.edu.in
*Corresponding author

Abstract: Hydrophobic materials are those which repel water molecules, the use of such material on aircraft surfaces can produce lower drag and higher lift compared to smooth finished surfaces, as the potential of reducing skin friction drag is much higher compared to other types of drag. The CFD studies for partly coated hydrophobic were carried out using ANSYS FLUENT software for different angles of attack such as 0°, 5°, 8°, 10°, 12°, 15° for various configurations such as No-Slip, Top-Slip, Rear-Slip and Bottom-Slip. Experiments were carried out with low-speed wind tunnel for the above angle of attack at 15 ms. The agreement between the computational results and experimental results is good. The results showed that out of all the four different configurations Bottom-Slip showed promising results. It provides a significant lift increase at lower angles. This is because the creation of the Laminar Separation Bubble near the trailing edge is delayed.

Keywords: hydrophobic; airfoil; lift; drag; surface coatings; anti-icing.

Reference to this paper should be made as follows: Khandai, S.C., Prasath, S. and Naveen, B. (2023) 'Computational and experimental analysis of partly coated hydrophobic airfoil', *Int. J. Computational Materials Science and Surface Engineering*, Vol. 11, Nos. 3/4, pp.211–232.

Biographical notes: Suresh Chandra Khandai obtained his Master's and Doctorate degree from Madras Institute of Technology, Anna University Chennai. He is currently working as Professor and Head of the Department of Aeronautical Engineering, Rajalakshmi Engineering College, Chennai, India. His research areas of interest are incompressible and compressible aerodynamics, high speed jet flows, propulsion, and computational fluid dynamics.

S. Prasath is an undergraduate student in the Department of Aeronautical Engineering, Rajalakshmi Engineering College, Chennai, India. His research areas of interest are low speed aerodynamics and computational fluid dynamics.

B. Naveen is an undergraduate student in the Department of Aeronautical Engineering, Rajalakshmi Engineering College, Chennai, India. His research areas of interest are experimental aerodynamics and computational fluid dynamics.

1 Introduction

Whenever an aircraft is in operation, whether it is in the air or on the ground, it is constantly subjected to four forces: thrust, weight, lift, and drag.

Thrust, Weight, Lift, and Drag are four forces that an aeroplane is constantly subjected to. The engine generates thrust, which is a forward force that aids in overcoming drag. Drag is the backward force created by the numerous airframe components obstructing the incoming airflow. The force acting perpendicular to the direction of airflow created by the aircraft's movement through the air is known as lift. The force of gravity pulling the aeroplane downward is known as weight. Engineers will concentrate on increasing thrust and lift at the same time to reduce weight and drag.

In this paper our main objective is to reduce the drag. When it comes to aircraft drag, there are many types such as form drag, skin-friction drag, interference drag, wave drag, induced drag and other few. During subsonic conditions, the predominant one is the skin friction drag, typically 40–50% of the total aircraft drag. Many techniques and methods are employed to reduce this drag.

Riblets (Figure 1) are grooved surfaces that are aligned with the incoming flow (Mele and Tognaccini, 2018). The goal of these grooved surfaces is to lower the turbulent boundary layer's skin friction drag. Wind tunnel tests have shown that riblets are particularly effective at reducing wall shear stress when their dimensions are tailored to the boundary layer's features. Flight tests have confirmed the conclusions found in the wind tunnel test.

Figure 1 Riblets

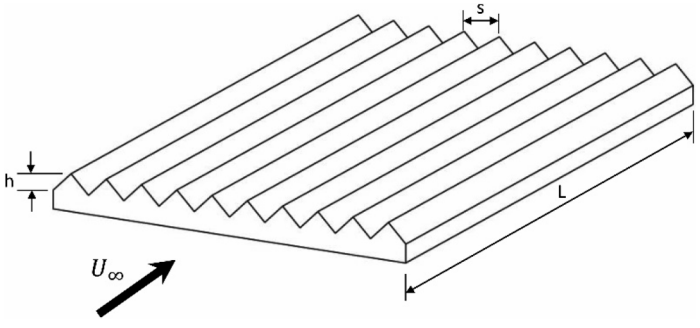

Boundary layer suction is a boundary layer control technique (Figure 2) in which an air pump collects and removes the boundary layer above the wing or at the aircraft's inlet. Fuel efficiency can be increased by up to 30% with this method. When the flow is laminar, or smooth, the air speed steadily increases in a continuous manner when the measurements are made away from the wing surface. In any case, the smooth laminar flow is disrupted by the boundary layer, which is separating from the surface and leading

to a low-pressure zone right behind the aerofoil. This low-pressure area has the effect of increasing total drag. People have attempted to delay the effect of flow separation through meticulous design and smooth surfaces over the years.

Figure 2 Boundary layer suction

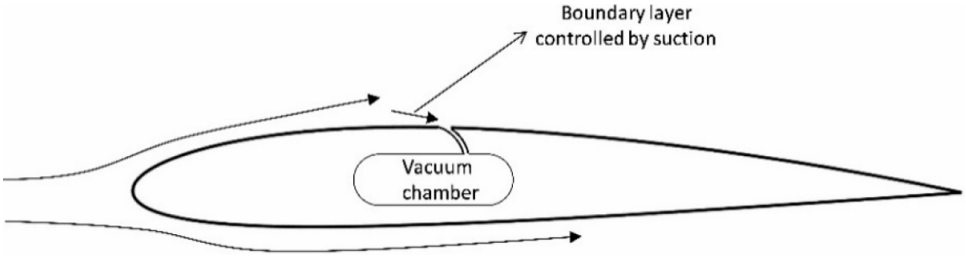

Boundary layer suction aims to extract the boundary layer that is above the surface before it can separate as a result of the velocity deficit caused by the boundary layer. Werner Pfenninger invented boundary layer suction technology during World War II, and it has been studied basically continuously since then.

The vortex generator (VG) (Figure 3), an aerodynamic device consisting of tiny vanes commonly affixed to an aircraft's surface or a wind turbine's rotor blade, is another approach for minimising skin-friction drag. When the VG is attached to a moving surface in the air, it creates a vortex by removing some of the slow-moving boundary layer that is in contact with the surface, delaying local flow separation and aerodynamic stalling, and thus improving the effectiveness of flaps, elevators, ailerons, and rudders.

Figure 3 Vortex generator (see online version for colours)

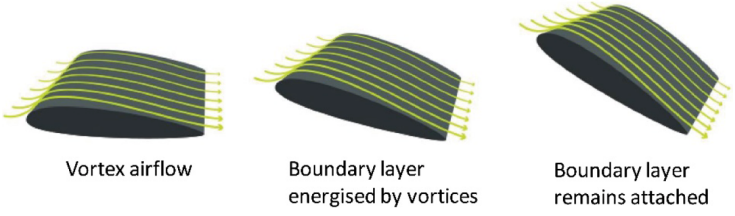

In this paper we focus on using a surface coated by a hydrophobic material which has the potential of reducing this drag and can also increase the lift. In addition to these benefits, it can also can prevent the formation of ice, as it is hydrophobic it can repel water particles hence can be used as an anti-icing agent.

Hydrophobic and Hydrophilic (Figure 4) materials are distinguished based on the geometry or shape of the water droplets when they are on a flat surface and correctly based on the angle that form between the underneath surface and the droplet's edge, which is known as the contact angle.

When water strikes a surface, it sometimes spreads evenly, and other times it forms small droplets. If the droplets spread across the surface, covering a larger area, and the contact angle is less than 90 degrees, the surface is known as a hydrophilic or water-liking surface. The surface is hydrophobic, or water-hating, if the droplet forms a spherical with very little contact with the surface and the contact angle is greater than 90 degrees. However, the nomenclature is not as straightforward. The majority of

hydrophobic and hydrophilic material research focuses on extreme circumstances, such as super hydrophobic and super hydrophilic materials.

Figure 4 Hydrophobic and hydrophilic

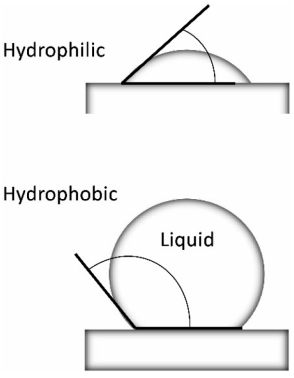

Super hydrophobic surfaces are those on which droplets establish a contact angle greater than 160 degrees. The surface is called super hydrophilic if the droplets are spread out flat with a contact angle of less than 20 degrees.

At a low Reynolds number, Lee et al. (2018) investigated the effects of a superhydrophobic surface on the flow around a NACA 0012 hydrofoil. They discovered that flow over a superhydrophobic surface has higher turbulence, which causes early vortex rollup in the wake and a reduction in vortex formation length. Nazemi et al. (2018) investigated wind tunnel experiment to gain a better understanding and prediction of the behaviour of PRT fabric in the wind tunnel. They discovered that surface roughness and the amount of it can have a significant impact on the drag reduction of PET fabric. Liu et al. (2018) investigated the use of soft PDMS materials for aircraft icing mitigation. They conclude that the much lower ice adhesion force over the PDMS surfaces (about 2 orders of magnitude lower than the baseline surface) would allow the aerodynamic stress from the airflow over the airfoil/wing surface to more likely sweep away the ice structures accreted on the airfoil surface covered with soft PDMS materials, as opposed to those accreted on the baseline surface of the airfoil/wing model. Qiu et al. (2019) researched the anti-ice properties of a low-wettability aero aluminium alloy. The investigation revealed that the anti-ice capability of aero aluminium alloy gradually improves with decreasing surface wettability. By using a direct numerical simulation technique, Rastegari and Akhavan (2018) explored the reduction of turbulent skin-friction drag with superhydrophobic (SH) longitudinal microgrooves and riblets. They discovered that super hydrophobic enabled direct numerical simulations to achieve drag reductions of up to 60% and up to 5%.

Seo and Mani (2016) used direct numerical simulation to investigate turbulence flow over super hydrophobic surfaces with micro-posts. They discovered a relation between slip velocity and shear in both the stream wise and lateral directions using pattern-averaged data. Sun and Huang (2020) used computational modelling to investigate the aerodynamic performance improvement of vertical-axis turbines with super-hydrophobic coated surfaces. The study discovered that an inflow velocity of 3 ms can increase maximum energy efficiency by 16.5%. You and Moin (2007) investigated the effect of a hydrophobic surface on the drag and lift of a circular cylinder numerically. Based on the

findings, a strategic hydrophobic surface treatment for reducing drag and RMS lift coefficients of a microscale bluff body can be developed. Hydrophobic surfaces reduce drag slightly in the laminar vortex shedding regime, primarily by reducing skin friction.

Experiments on the ability of the liquid-infused surfaces to decrease turbulent flow drag were carried out by Van Buren et al. (2017). They discovered that super hydrophobic surfaces reduced drag in turbulent Tylor-couette flow by 45% and liquid-infused surfaces by up to 35%. With increasing viscosity ratio, groove width, fluid area friction, and Reynolds number, the amount of drag was reduced. At the fluid-solid interface, Rothstein (2010) investigated the effects of surface roughness and hydrophobicity slip. The investigation's findings demonstrated that super hydrophobic drag reduction increases with flow rate and Reynolds number in both laminar and turbulent flows. Park et al. (2013), Daniello et al. (2009) and Martell et al. (2009) investigated the effects of super hydrophonic surface on skin-friction drag in turbulent flow. They discovered a strong correlation between the effective slip length normalised by viscous wall units and the drag decrease in turbulent flows.

The effects of a hydrophobic coating on a NACA 2412 airfoil were studied numerically and experimentally in the current research work. We are interested in understanding the detailed aerodynamic effects of the partly coated hydrophobic bottom surface on the flow fields at various angles of attacks. This research will improve the understanding of the flow physics of partially coated surfaces with various self-cleaning and anti-icing properties.

2 Computational analysis

Direct simulations are impossible due to the scale length (microns) of hydrophobic materials. An appropriate wall boundary condition based on the slip length idea can be used to describe hydrophobic surfaces. This slip length concept has been employed and has led to effective and accurate results (Chini et al., 2017).

This same concept was used by Chini for numerical investigation of super hydrophobic surfaces to increase airfoil performance. This was done by replacing the no-slip airfoil with 50% slip airfoil, the total lift increases by up to 66% for $\alpha = 0°$. For larger α values, using 50% slip airfoil is still promising but not as efficient. For example, when $\alpha = 15°$, total lift increase by 31%. It should be noted that 50% slip velocity on the wall is easily achievable on a super hydrophobic surface (Lee et al., 2018).

Our intention was to make the super hydrophobic airfoil effective even at higher angles of attack.

2.1 Methodology

A Navier slip length boundary condition is commonly used to parameterise the effect of a super hydrophobic surface at the macroscopic level.

$$U_s = \beta \frac{\partial U_t}{\partial n} \tag{1}$$

where U_t is tangential velocity and U_s is the slip velocity, which is proportional to the slip length β and the velocity derivative.

The challenge for curved surfaces is that the direction of slip velocity (which is tangent to the airfoil) and velocity gradient (which is normal to the airfoil) both change along the airfoil's surface.

The procedure of developing the user defined function (UDF) is as follows:

$$U_s = \beta \frac{\partial U_t}{\partial n} \tag{2}$$

The velocity gradient normal to the airfoil surface can be found as:

$$\frac{\partial U_t}{\partial n} = \hat{n} \cdot \nabla U_t \tag{3}$$

Where n is the normal unit vector to the airfoil and ∇U_t in Cartesian coordinates is

$$\nabla U_t = \frac{\partial U_t}{\partial x}\hat{i} + \frac{\partial U_t}{\partial y}\hat{j} + \frac{\partial U_t}{\partial z}\hat{k} \tag{4}$$

Assuming a two-dimensional flow, and considering the velocity angle at any point on the airfoil's surface θ (as illustrated in Figure 5), the unit vectors along the tangential (t) and normal (n)) directions (as shown in Figure 6) can be represented as:

$$\hat{n} = \cos\varphi\hat{I} + \sin\varphi\hat{J} \tag{5}$$

$$\hat{t} = \cos\theta\hat{I} + \sin\theta\hat{J} \tag{6}$$

$$\hat{n} = -\sin\theta\hat{I} + \cos\theta\hat{J} \tag{7}$$

$$\frac{\partial U_t}{\partial n} = \hat{n} \cdot \left(\frac{\partial U_t}{\partial x}\hat{i} + \frac{\partial U_t}{\partial y}\hat{j} + \frac{\partial U_t}{\partial z}\hat{k} \right) \tag{8}$$

Substituting equation (4), equation (8) can be written as

$$\frac{\partial U_t}{\partial n} = (-\sin\theta\hat{I} + \cos\theta\hat{J}) \cdot \left(\frac{\partial U_t}{\partial x}\hat{i} + \frac{\partial U_t}{\partial y}\hat{j} + \frac{\partial U_t}{\partial z}\hat{k} \right) \tag{9}$$

$$\frac{\partial U_t}{\partial n} = -\sin\theta\frac{\partial U_t}{\partial x} + \cos\theta\frac{\partial U_t}{\partial y} \tag{10}$$

Resolving for velocities, we obtain:

$$U_t = u\cos\theta + v\sin\theta \tag{11}$$

substituting equation (11) in equation (9), we have:

$$\frac{\partial U_t}{\partial n} = -\sin\theta\frac{\partial}{\partial x}(u\cos\theta + v\sin\theta) + \cos\theta\frac{\partial}{\partial y}(u\cos\theta + v\sin\theta) \tag{12}$$

And with the velocity gradient, the UDF for the magnitude of the slip velocity is developed as follows:

$$U_s = \beta\left(-\sin\theta\frac{\partial}{\partial x}(u\cos\theta + v\sin\theta) + \cos\theta\frac{\partial}{\partial y}(u\cos\theta + v\sin\theta) \right) \tag{13}$$

Figure 5 Freestream velocity over the airfoil (see online version for colours)

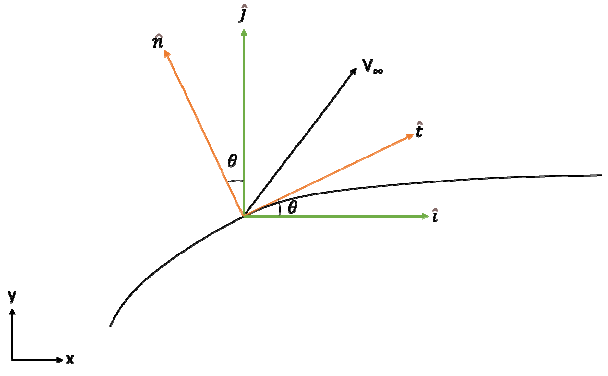

Figure 6 Projections of velocity components (see online version for colours)

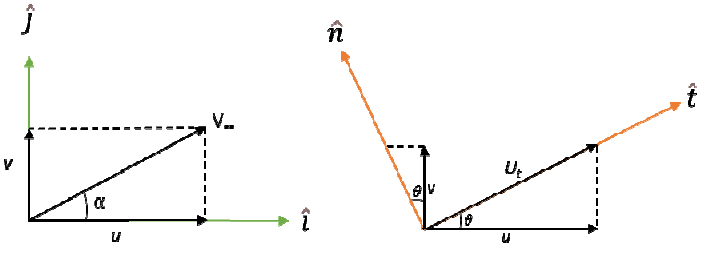

Figure 7 2-D computational domain around the airfoil

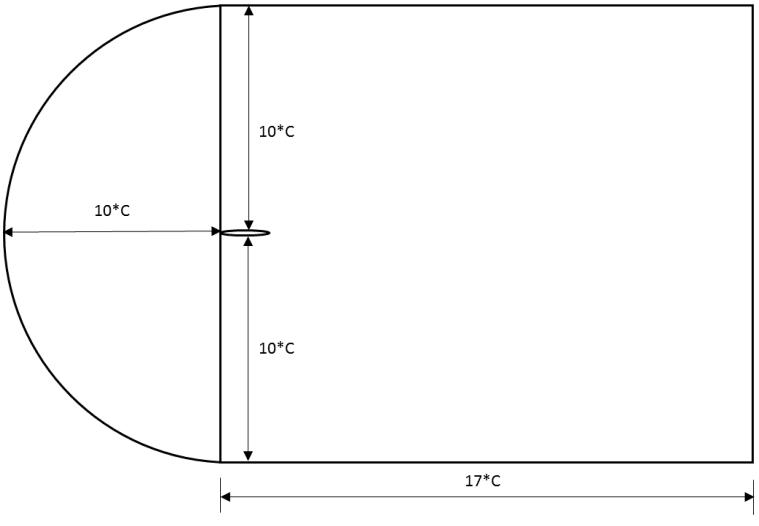

2.2 Domain generation

A standard NACA 2412 airfoil was chosen for analysis using ANSYS. The computational domain around the airfoil was generated in ANSYS design module.

A C-shaped domain was generated and dimensions are mentioned in terms of the chord length '*c*' and shown in Figure 7.

2.3 Mesh generation

A structure mesh was generated in the computational domain by using ANSYS- ICEM software. The mesh was made finer in the critical region like around the airfoil. The minimum element size around the airfoil was 1.5 micros. The grid had total 0.41 million (4.1 lakhs) nodes. The average skewness of the grid was 0.85. Figure 8 shows that grid independence study. Figure 9 shows the structured mesh around the airfoil.

Figure 8 Lift coefficient at 12º angle of attack no-slip condition against number of grid cells

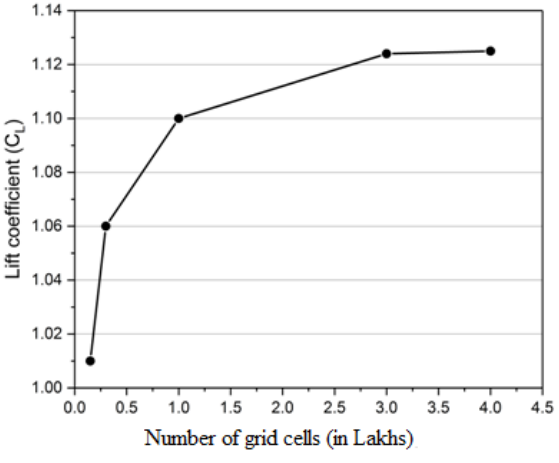

Figure 9 C-shape mesh around NACA 2412 airfoil and enlarged view of the airfoil (see online version for colours)

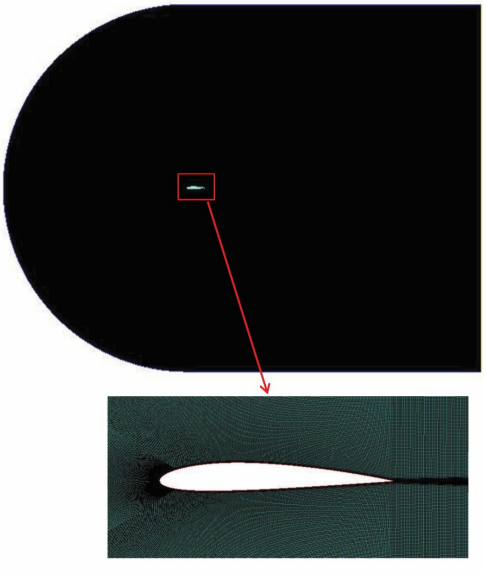

2.4 Solver configuration

The pressure-based solver and Standard k-omega model was used. This model was used as it yielded accurate results than any other models.

The Wilcox k-model is the foundation for ANSYS FLUENT's standard k-model, which includes low-Reynolds-number effects, compressibility, and shear flow spreading corrections. Free shear flow spreading rates predicted by the Wilcox model are remarkably similar to data for far wakes, mixing layers, and plane, round, and radial jets, making it acceptable for both wall-bounded and free shear flows.

The standard k-model is an empirical model based on model transport equations for turbulent kinetic energy (k) and specific dissipation rate (ω), which is generally referred to as the ratio of ε to k. As the k-model has been revised throughout time, production terms have been added to both the k and equations, enhancing the model's accuracy in predicting free shear flows.

The following transport equations yield the turbulent kinetic energy, k, and the specific dissipation rate ω,

$$\frac{\partial}{\partial t}(\rho k) + \frac{\partial}{\partial x_i}(\rho k u_i) = \frac{\partial}{\partial x_j}\left(\Gamma_k \frac{\partial k}{\partial x_j}\right) + G_k - Y_k + S_k \tag{14}$$

and

$$\frac{\partial}{\partial t}(\rho w) + \frac{\partial}{\partial x_i}(\rho w u_i) = \frac{\partial}{\partial x_j}\left(\Gamma_w \frac{\partial w}{\partial x_j}\right) + G_w - Y_w + S_w \tag{15}$$

In these equations, G_k represents the generation of turbulence kinetic energy due to mean velocity gradients. G_ω represents the generation of ω. Γ_k and Γ_ω represent the effective diffusivity of k and ω, respectively. Y_k and Y_ω represent the dissipation of k and ω due to turbulence. All the above terms are calculated as described below. S_k and S_ω are user-defined source terms.

G_k denotes the generation of turbulent kinetic energy due to mean velocity gradients in these equations. G_ω stands for the generation of ω. The effective diffusivity of k and ω, respectively, is represented by Γ_k and Γ_ω. The dissipation of k and ω due to turbulence is represented by Y_k and Y_ω. All of the terms listed above are calculated as follows. User-defined source terms are S_k and S_ω.

2.5 Boundary conditions

The incident angle of the free stream air flow having a velocity magnitude of 15 ms was varied by altering the vertical and horizontal velocity components Vx & Vy, which is easier and quicker rather than altering the geometry. The outlet conditions and the operating condition are set to standard atmospheric conditions of 101325 Pa pressure, 1.29 kg/m^3 density and 288 K temperature. Figure 10 shows that the boundary conditions imposed at various locations.

Figure 10 Boundary conditions imposed at various locations (see online version for colours)

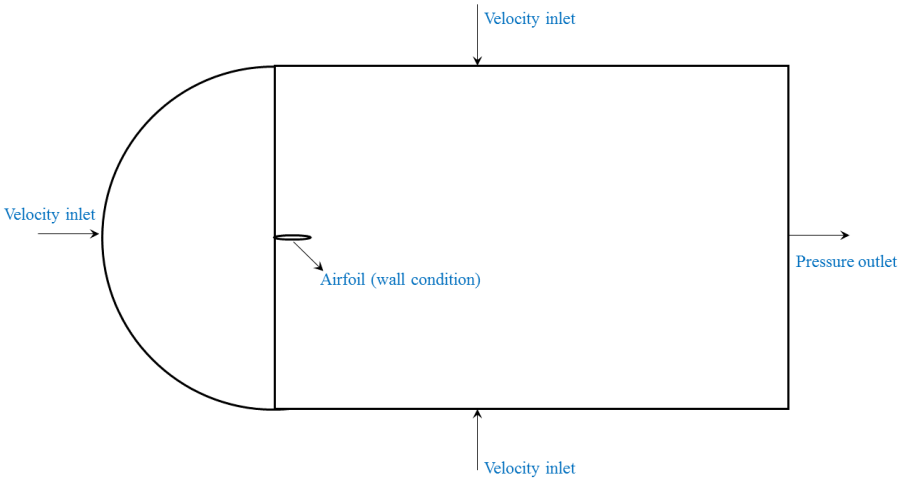

3 Experimental analysis

CFD is an add-on tool for better understanding the flow. CFD can provide a broad qualitative (colour plots) or quantitative (numerical data) idea of the physics under consideration. CFD will be helpful at the preliminary design stage, when several designs must be examined for performance. It is important to note that CFD is not a substitute for experimental or analytical methods. This method contains numerous errors (such as discretisation, rounding, and algorithm problems). Once we get the CFD results, we must validate them either using experimental results, analytical data, or both. Once a few prototypes have been chosen, we may conduct experiments on solely those designs to assess their performance and validate our CFD results. This reduces the cost and time required to analyse all initial concepts.

For aerodynamic experimentation typically a wind tunnel is used. Based on the size of the model and conditions in which it is be tested, the required type of wind tunnel will be selected. The wind tunnel used for the current experiment is specified in Table 1. A photograph of laboratory tested model was fitted in the wind tunnel is shown in Figure 11.

Table 1 Specifications of the wind tunnel facility

Type of tunnel	*Suction type, low speed, open circuit*
Type of test section	300 × 300 mm, Acrylic Windows
Max. Velocity	40 ms
Drive	Axial Flow; Fan Driven by AC Motor Kirloskar Make 7.5HP, 1500 RPM with AC drive for speed control
Force measurement	3 Component Force balance
Pressure measurement	13 Port Multi-Tube Manometer
Flow visualisation	Smoke generator

Figure 11 Wing model in the test section (see online version for colours)

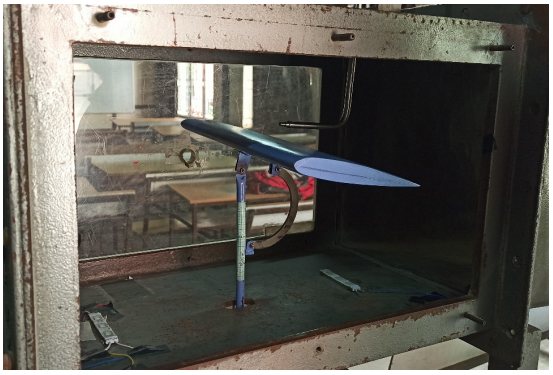

3.1 Procedure

A 3D CAD model of the NACA 2412 airfoil was designed using Autodesk Fusion 360. Two identical models were fabricated to compare the performance of the hydrophobic surface. One of the models was coated with the Polyurethane based hydrophobic surface coating on its bottom surface as suggested by CFD results.

The Wind tunnel and the force balance were calibrated and checked for instrumental errors before performing the experimentation. Each of the models were mounted on the wind tunnel and tested for various angles of attacks such as 0°, 5°, 8°, 10°, 12°, 15° and the lift and drag were obtained simultaneously. The operating conditions were set at standard environment conditions and inlet velocity was kept around 15 ms, which produces a flow Reynolds number of 1,53,323 to conform with our wind tunnel capabilities.

4 Results and discussions

4.1 Computational results

The CFD analysis was conducted for various angles of attacks such as 0°, 5°, 8°, 10°, 12°, 15° and the coefficient of lift and coefficient of drag were obtained simultaneously. The outlet conditions and the operating condition are set to standard atmospheric conditions of 101325 Pa. Different configurations as shown in Figure 12 were tested with the slip condition applied on different parts such as top, bottom, and rear portions of airfoil.

Figure 12 Wing tunnel facility (see online version for colours)

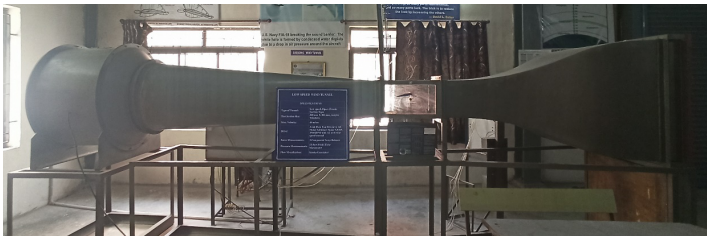

The comparison of coefficient of lift, coefficient of drag, and L/D for various boundary conditions at various angles of attack is shown in Tables 2–4.

Table 2 C_L for different configurations at various angle of attack

α	*No-Slip*	*Rear Slip*	*Top Slip*	*Bottom Slip*
0°	0.228	0.21	0.37	0.24
5°	0.78	0.81	0.89	0.76
8°	1.02	1.1	0.95	0.98
10°	1.17	0.98	1.09	1.19
12°	1.26	0.91	1.17	1.27
15°	0.912	0.83	0.89	0.99

Table 3 C_D for different configurations at various angle of attack

α	*No-Slip*	*Rear Slip*	*Top Slip*	*Bottom Slip*
0°	0.022	0.023	0.017	0.018
5°	0.039	0.032	0.029	0.029
8°	0.049	0.032	0.039	0.032
10°	0.072	0.10	0.071	0.072
12°	0.098	0.135	0.11	0.094
15°	0.16	0.19	0.18	0.17

Table 4 L/D for different configurations at various angle of attack

α	*No-Slip*	*Rear Slip*	*Top Slip*	*Bottom Slip*
0°	10.36	9.13	21.76	13.33
5°	20	25.31	30.68	26.20
8°	20.81	34.73	24.35	30.62
10°	16.25	9.8	15.35	16.52
12°	12.85	6.74	10.63	13.51
15°	5.7	4.36	4.94	5.82

Here, Figures 14–19 shows the velocity contour of No-Slip airfoil. Figures 14–19 represents the velocity contours at various angle and attack. In Figure 13 due to no-slip condition the velocity is zero at the aerofoil wall.

Figure 13 Different slip configurations (see online version for colours)

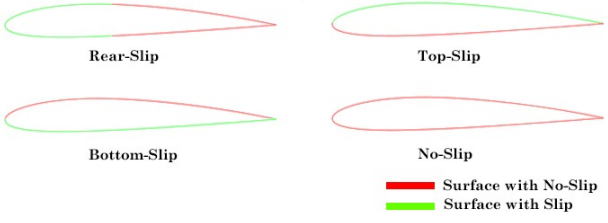

Figure 14 Velocity contour of no-slip configuration at 0° AoA (see online version for colours)

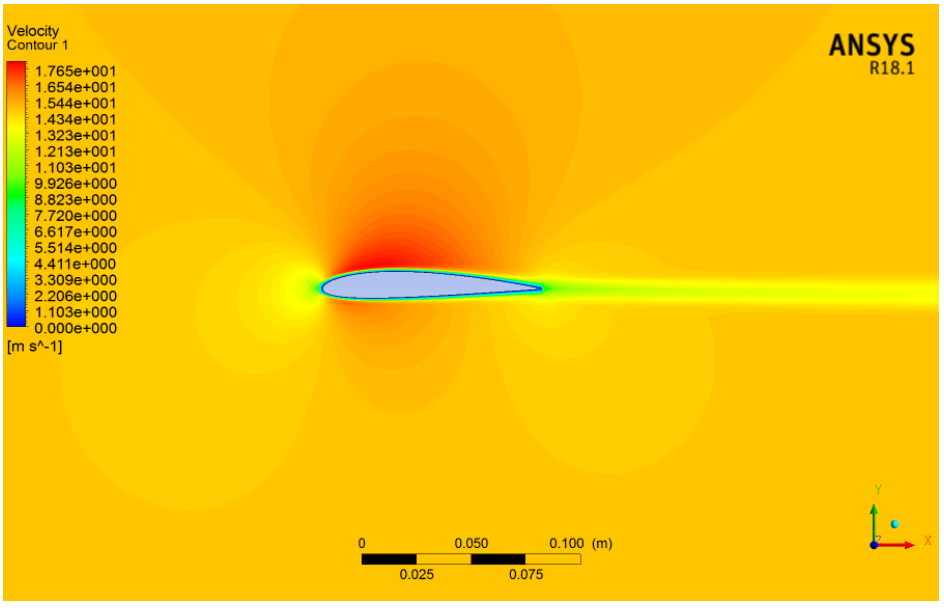

Figure 15 Velocity contour of no-slip configuration at 5° AoA (see online version for colours)

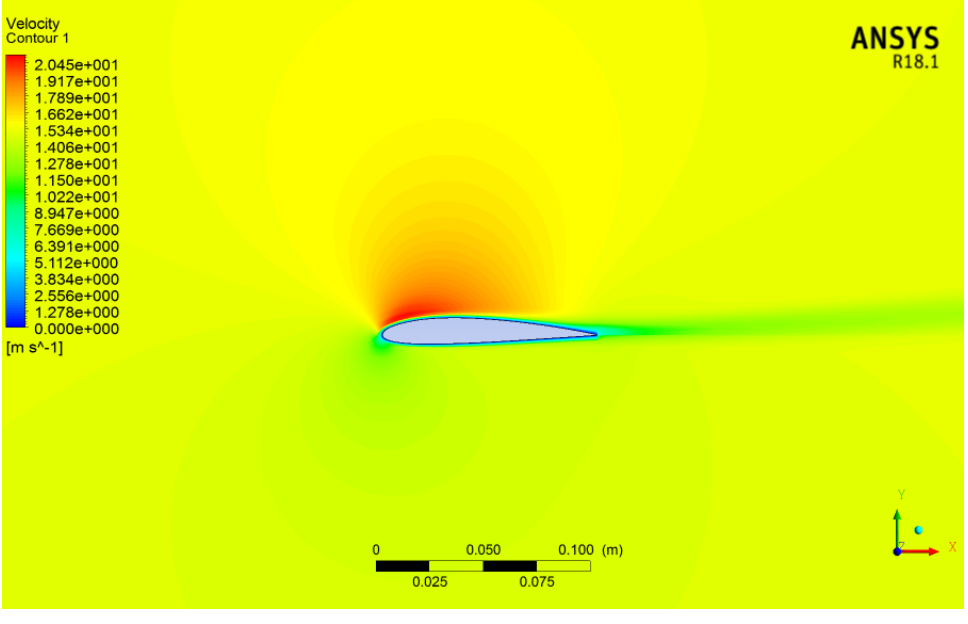

Figure 16 Velocity contour of no-slip configuration at 8° AoA (see online version for colours)

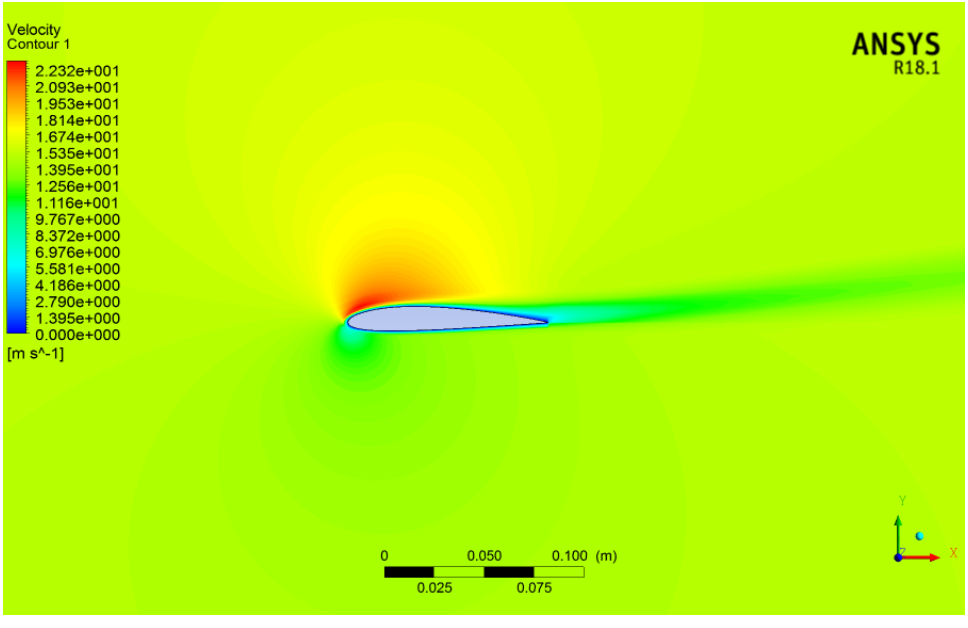

Figure 17 Velocity contour of no-slip configuration at 10° AoA (see online version for colours)

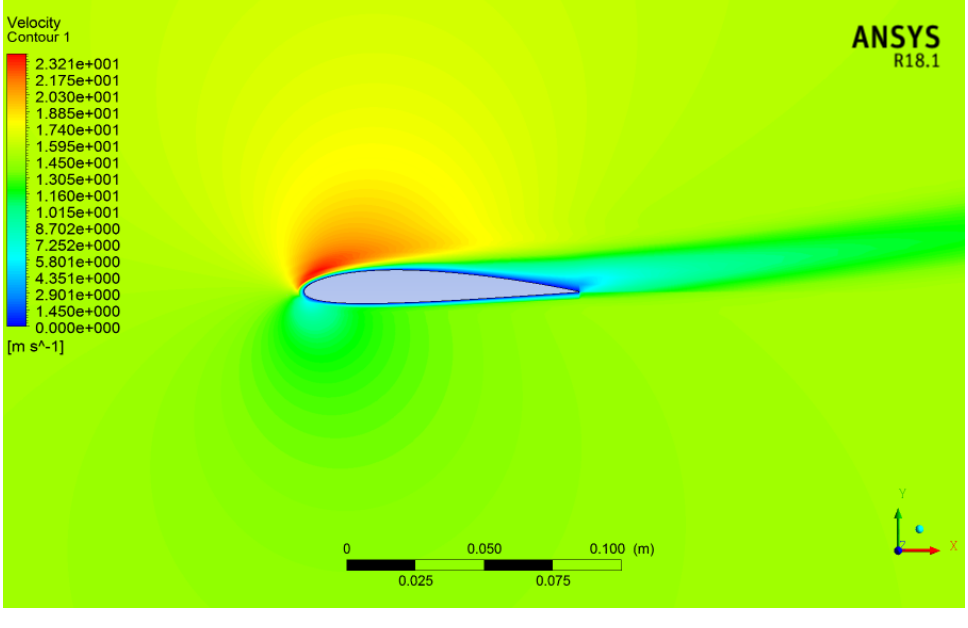

Figure 18 Velocity contour of no-slip configuration at 12° AoA (see online version for colours)

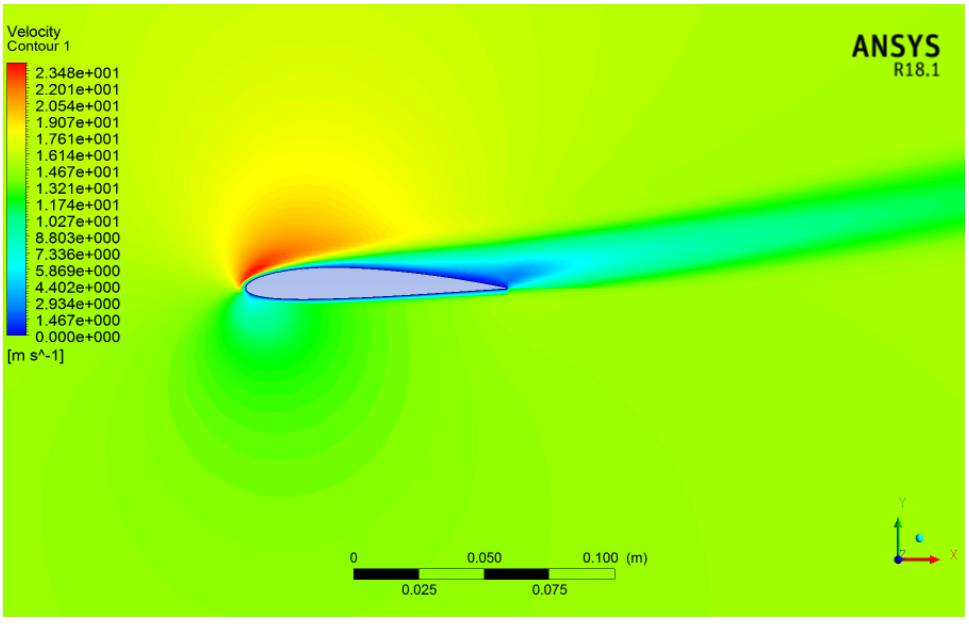

Figure 19 Velocity contour of no-slip configuration at 15° AoA (see online version for colours)

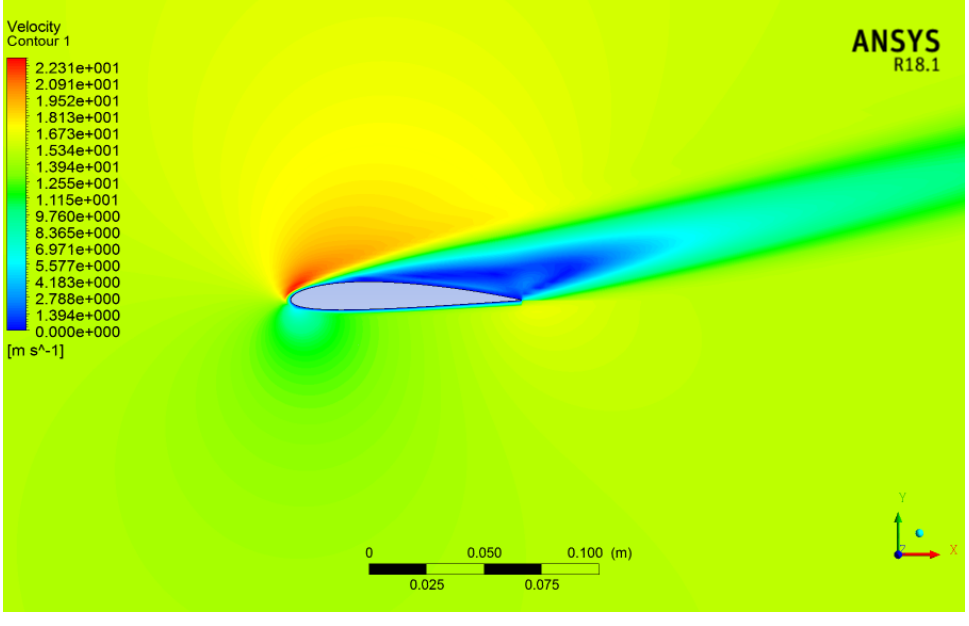

This is related to the creation of a laminar separation bubble, which occurs when flow separation occurs at greater angles of attack. However, the development of this laminar separation bubble takes longer in hydrophobic coated aerofoils than in No-Slip aerofoils, implying that hydrophobic coated aerofoils perform better.

Figures 20–22 shows the coefficient of lift, coefficient of drag and Lift-to-Drag ratio. From the results, we can say that the Top-Slip configuration offers more lift increment at lower angles of attack. But at higher angles, the performance is poor compared to No-Slip aerofoil. Even though the Rear-Slip configuration produces more lift compared to No-Slip, the stall angle is far below the No-Slip aerofoil, which is not favourable. Furthermore, at greater angles of attack, the performance of the Bottom-Slip design is essentially identical to that of the No-Slip aerofoil. On the other hand, it provides a significant lift increase at lower angles.

Figure 20 C_L vs alpha curve for various boundary conditions (see online version for colours)

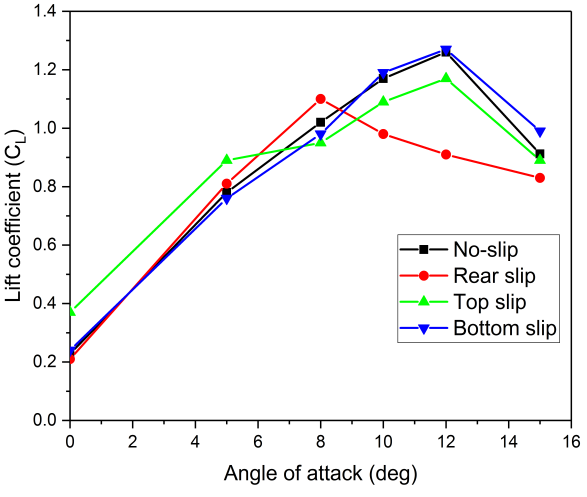

Figure 21 C_D vs alpha curve for various boundary conditions (see online version for colours)

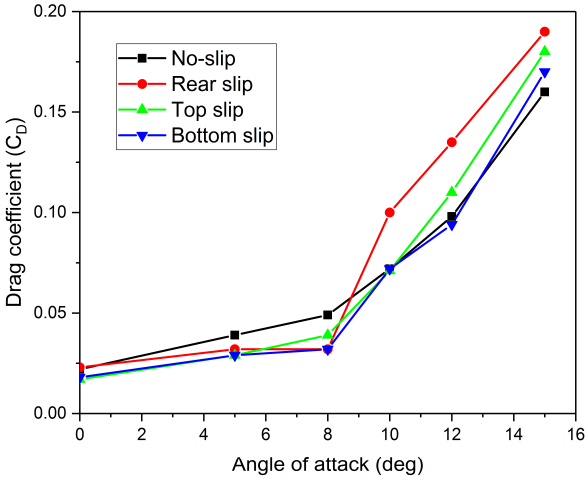

Figure 22 L/D vs alpha curve for various boundary conditions (see online version for colours)

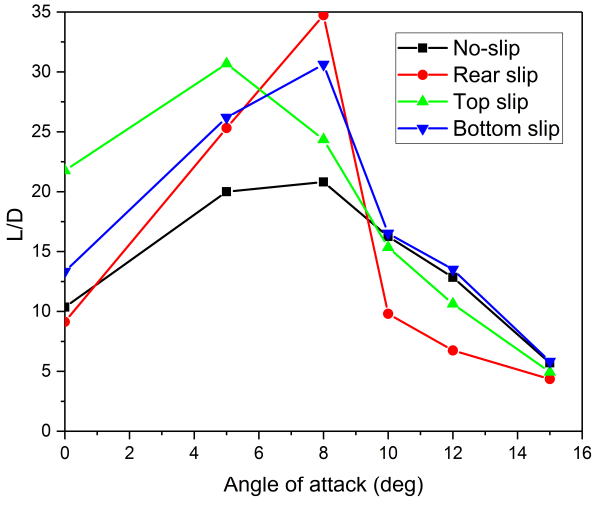

4.2 Experimental results

The obtained values of lift and drag were converted to corresponding coefficients and plotted against the angle of attack and C_L vs α and C_D vs α curves were obtained.

The comparison of coefficient of lift, coefficient of drag, and L/D for various boundary conditions at various angles of attack is shown in Tables 5 and 6.

Table 5 Experimental results for no-slip model

AOA (deg)	*Lift* (N)	*Drag* (N)	C_L	C_D	*L/D*
0	1.393	0.294	0.232	0.049	4.733
5	5.690	0.326	0.949	0.054	17.470
8	7.387	0.390	1.232	0.065	18.920
10	8.054	0.379	1.343	0.063	21.269
12	8.849	0.608	1.476	0.101	14.548
15	4.905	1.777	0.818	0.296	2.761

Table 6 Experimental results for bottom-slip model

AOA (deg)	*Lift* (N)	*Drag* (N)	C_L	C_D	*L/D*
0	1.530	0.275	0.255	0.046	5.571
5	6.965	0.245	1.162	0.041	28.400
8	8.397	0.334	1.401	0.056	25.176
10	8.849	0.334	1.476	0.056	26.529
12	9.938	0.510	1.657	0.085	19.481
15	4.905	1.864	0.818	0.311	2.632

Figures 23–25 shows the coefficient of lift, coefficient of drag and Lift-to-Drag ratio. From the results, we can say that the Top-Slip configuration offers more lift increment at lower angles of attack. But at higher angles, the performance is poor compared to No-Slip aerofoil. Even though the Rear-Slip configuration produce more lift compared to No-Slip, the stall angle is far below the No-Slip aerofoil, which is not favourable. Moreover, at higher angles of attack, the Bottom-Slip configuration performs almost as well as a No-Slip aerofoil. Nevertheless, at lower angles, it offers a significant lift increase.

Figure 23 C_L vs alpha curve for bottom-slip and no-slip models (see online version for colours)

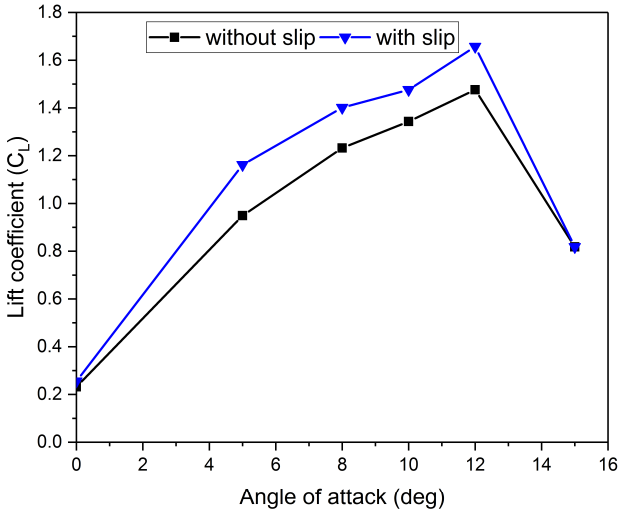

Figure 24 C_D vs alpha curve for bottom-slip and no-slip models (see online version for colours)

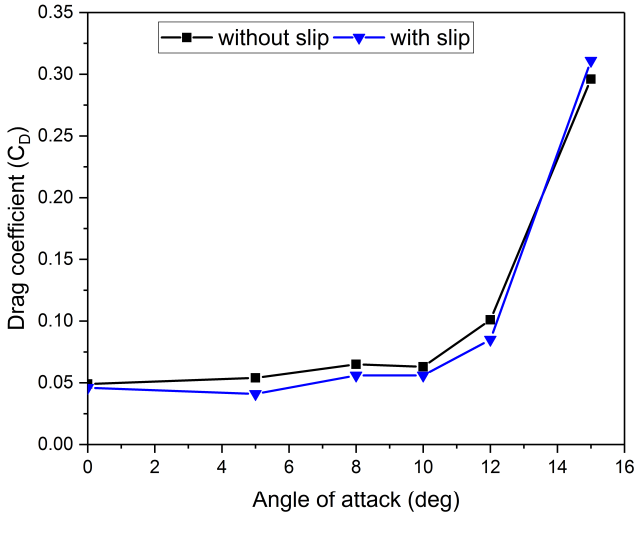

Figure 25 L/D vs alpha curve for bottom-slip and no-slip models (see online version for colours)

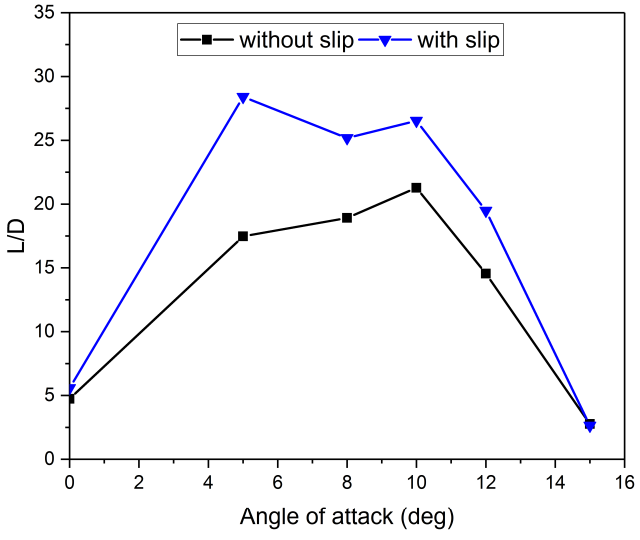

4.3 Validation

The distinctions between a code, simulation, and model must first be understood. In essence, one converts a model into computer code, which is then utilised to run a CFD simulation, yielding numbers for engineering analysis. Verification and validation analyse the code and simulation results for errors. Acceptable amounts of uncertainty and inaccuracy are required to get credibility. Validation evaluates whether the computational simulation matches physical reality. It assesses the models' science by comparing them to experimental results.

Professionals dispute on the specific processes for CFD simulation verification and validation. CFD is becoming more mature, yet it is still a new technique. CFD is a sophisticated technology that uses highly coupled nonlinear partial differential equations to simulate theoretical and practical models in a discrete domain with a complicated geometric structure. The three roots of CFD: theory, experiment, and computing must all be included in a careful assessment of mistakes and uncertainties. Furthermore, as computer resources increase, CFD applications are rapidly developing.

In CFD, there are plenty of mathematical models available to compute the results. However, the one that comes close to actual results must be used. So, the pressure-based solver and Standard k-omega model was used as these yielded accurate results. The obtained experimental results were compared with the CFD simulation results shown in Table 8 as well as the theoretical values obtained from the XFOIL software shown in Table 7.

Observing the results obtained from CFD, Xfoil and experimentation, we can see that experimentation results of coefficient of lift in Figure 26 and coefficient of drag in Figure 27 vary slightly when compared to CFD and Xfoil results. This can be due to various reasons such as approximations done during CFD which leads to certain errors and the wind tunnel results can be influenced by various physical factors.

Figure 26 C_L vs alpha (see online version for colours)

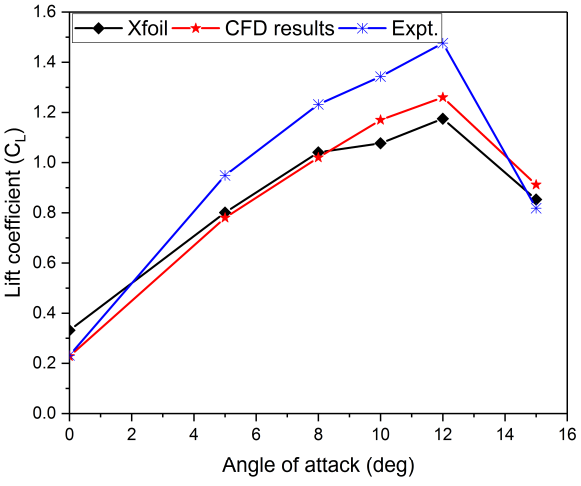

Figure 27 C_D vs alpha (see online version for colours)

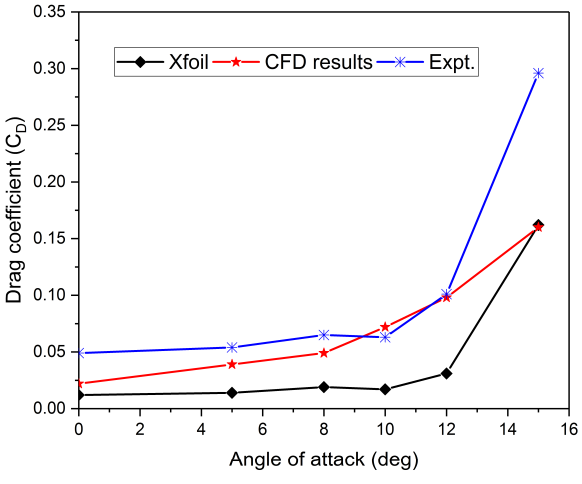

Table 7 Results obtained from XFOIL software

AoA (deg)	C_L	C_D	*L/D*
0	0.332	0.012	27.66
5	0.801	0.014	57.21
8	1.041	0.019	54.79
10	1.077	0.017	63.35
12	1.175	0.031	37.90
15	0.853	0.162	5.26

Table 8 Results obtained from CFD

AoA (deg)	C_L	C_D	*L/D*
0	0.228	0.022	10.36
5	0.78	0.039	20
8	1.02	0.149	20.81
10	1.17	0.072	16.25
12	1.26	0.098	12.85
15	0.912	0.16	5.7

The results obtained from CFD and Experimentation for different slip configurations and for different angles of were studied and inferred in the following chapter.

5 Conclusions

CFD tests for partly coated hydrophobic paints were conducted for various angles of attack such as 0°, 5°, 8°, 10°, 12°, and 15° for various configurations such as No-Slip, Top-Slip, Rear-Slip, and Bottom-Slip, and the results obtained led to the following conclusions.

- Out of all the four configurations Bottom-Slip showed the highest C_{Lmax} which is 1.06 at 12° angle of attack.
- At greater angles of attack, the performance of the Bottom-Slip configuration is essentially identical to that of the No-Slip aerofoil. On the other hand, it provides a significant lift increase at lower angles. This is because the creation of the Laminar Separation Bubble near the trailing edge is delayed.
- The maximum percentage difference of L/D occurs at the angles of attack of 5° and 8° which are 80% and 40% respectively.

The CFD studies led us to the fact that bottom-slip configuration is better than the other configurations, so we proceeded on with the experimentation using bottom-slip configuration. The maximum percentage difference of L/D occurs at the angles of attack of 5° and 8° similar to CFD results which are 63% and 33% respectively.

References

Chini, S.F., Mahmoodi, M. and Nosratollahi, M. (2017) 'The potential of using super hydrophobic surfaces on airfoils and hydrofoils: a numerical approach', *Int. J. Computational Materials Science and Surface Engineering*, Vol. 7, No. 1, pp.44–61.

Daniello, R.J., Waterhouse, N.E. and Rothstein, J.P. (2009) 'Drag reduction in turbulent flows over superhydrophobic surfaces', *Physics of Fluids*, Vol. 21, p.085103, https://doi.org/10.1063/1.3207885

Lee, J., Kim, H. and Park, H. (2018) 'Effects of superhydrophobic surfaces on the flow around an NACA0012 hydrofoil at low Reynolds numbers', *Exp Fluids*, Vol. 59, p.111.

Liu, Y., Ma, L., Wang, W., Kota, A.K. and Hu, H. (2018) 'An experimental study on soft PDMS materials for aircraft icing mitigation', *Applied Surface Science*, Vol., 447, pp.599–609.

Martell, M.B., Perot, J.B. and Rothstein, H.P. (2009) 'Direct numerical simulations of turbulent flows over superhydrophobic surfaces', *Journal of Fluid Mechanics*, Vol. 620, pp.31–41, doi: 10.1017/S0022112008004916.

Mele, B. and Tognaccini, R. (2018) 'Slip length–based boundary condition for modeling drag reduction devices', *AIAA Journal*, Vol. 56, No. 9.

Nazemi, S., Khajavi, R., Rabie Far, H., Yazdanshenas, M.E. and Raad, M. (2018) 'Modeling and simulation of drag force for coated PET fabric with silica nano particles', *International Journal of Clothing Science and Technology*, Vol. 30, No. 3, pp.398–411.

Park, H., Park, H. and Kim, J. (2013) 'A numerical study of the effects of superhydrophobic surface on skin-friction drag in turbulent channel flow', *Physics of Fluids*, Vol. 25, p.110815, doi: 10.1063/1.4819144.

Qiu, C.H., Cheng, C.C. and M., Li (2019) 'Analysis on anti-ice properties of aero aluminum alloy with weak wettability', *IOP Conference Series: Materials Science and Engineering*, Vol. 479, Nos. 1–8, p.012059, IOP Publishing.

Rastegari, A. and Akhavan, R. (2018) 'The common mechanism of turbulent skin-friction drag reduction with superhydrophobic longitudinal microgrooves and riblets', *J. Fluid Mech*., Vol. 838, pp.68–104, doi: 10.1017/jfm.2017.865.

Rothstein, J.P. (2010) 'Slip on superhydrophobic surfaces', *Annual Review of Fluid Mechanics*, Vol. 42, pp.89–109, doi: 10.1146/annurev-fluid-121108-145558.

Seo, J. and Mani, A. (2016) 'On the scaling of the slip velocity in turbulent flows over superhydrophobic surface', *Physics of Fluids*, Vol. 28, p.025110, doi: 10.1063/1.4941769.

Sun, J. and Huang, D. (2020) 'Numerical investigation on aerodynamic performance improvement of vertical-axis tidal turbine with super-hydrophobic surface', *Ocean Engineering*, Vol. 217, p.107995, https://doi.org/10.1016/j.oceaneng.2020.107995

Van Buren, T. and Smits, A.J. (2017) 'Substantial drag reduction in turbulent flow using liquid-infused surface', *Journal of Fluid Mechanics*, Vol. 827, pp.448–456, doi: 10.1017/jfm. 2017.503.

You, D. and Moin, P. (2007) 'Effects of hydrophobic surface on the drag and lift of a circular cylinder', *Physics of Fluids*, Vol. 19, p.081701, doi: 10.1063/1.2756578.